Interaction-time-averaged optical pumping in alkali-metal-atom Doppler spectroscopy

Thomas Lindvall* and Ilkka Tittonen
Micro and Nanosciences, Micronova, Helsinki University of Technology, P.O. Box 3500, FI-02015 TKK, Finland
(Received 9 July 2009; published 9 September 2009)

We study the influence of optical pumping on Doppler-broadened alkali-metal-atom D line spectra by solving the time-dependent density matrix for an open two-level system. The time-dependent absorption is averaged over the distribution of interaction times obtained from the three-dimensional beam geometry and atomic velocity distribution and over the longitudinal velocity distribution. The optical pumping is significant at much lower intensities than saturation and depends strongly on the intensity, beam radius, vapor cell length, and spontaneous-decay branching ratio. The result is in agreement with our earlier steady-state solution for a wide range of parameters and predicts two interesting line-shape features.

DOI: 10.1103/PhysRevA.80.032505 PACS number(s): 32.30.Jc, 32.70.Jz, 32.80.Xx, 42.62.Fi

I. INTRODUCTION

Alkali-metal atoms have long been studied in atomic and optical physics due to several beneficial properties: with a single valence electron they have a relatively simple level structure, the wavelengths of their D lines lie in the visible and near-infrared, where diode lasers are readily available, and their relatively high vapor pressures allow significant absorption at room temperature as well as simple generation of atomic beams. Applications span from technical to scientific: frequency stabilization of lasers [1], atomic frequency standards and atomic clocks [2], atomic magnetometers [3], laser cooling [4–6], Bose-Einstein condensation [7,8], coherent population trapping [9], and controlling the propagation of light [10]. All of these applications require detailed knowledge of the atomic spectra and their dependence on the experimental parameters.

Even though optical pumping [11] has been known for a long time, there has been a lot of recent interest in the fundamental aspects of optical pumping in alkali-metal atoms. Vanier [12] has analyzed its influence in the case of strong collisional broadening by an inert buffer gas in an atomic clock based on coherent population trapping. The influence of optical pumping on saturated absorption spectra has been studied by two different groups [13,14] and the influence on the Doppler-broadened absorption of the rubidium D lines has been experimentally studied by Siddons *et al.* [15].

In a recent paper [16] we showed how optical pumping affects Doppler-broadened alkali-metal-atom spectra at intensities much lower than saturation. The effect of a finite laser beam radius and collisions with the glass-cell walls was accounted for as ground-state relaxation allowing us to use the steady-state solutions for the density matrix. However, as pointed out in [13], optical pumping is really a transient effect and the absorption should be averaged over the range of interaction times between the atoms and the laser field.

In this paper, we solve the time-dependent density matrix equations numerically and derive a practical and accurate analytical approximation. We derive a distribution for the interaction time taking into account the three-dimensional distribution of atoms and their velocity distribution. By weighting the time-dependent solution with this distribution, we show that the result from [16] is valid over a wide range of parameters. Two interesting line-shape features are also predicted: the velocity-dependent homogeneous line shapes of the atoms are no longer Lorentzian due to optical pumping, and for beam diameters comparable to the cell length, a dip is created in the Doppler-broadened spectrum.

II. THEORY

As described in our earlier work [16], we reduce the alkali-metal atom level structure to a three-level model by assuming that the laser field only couples one hyperfine excited state at a time and by averaging over all relevant magnetic sublevels. Figure 1 shows how this effective three-level system is formed for σ^+ excitation of the $|F=1\rangle \rightarrow |F'=1\rangle$ transition in an atom with a nuclear spin $I=1/2$. The transition strength C^2 and the branching ratios A_g (A_n) of spontaneous emission from the excited state $|e\rangle$ to the ground state $|g\rangle$ (noncoupled state $|n\rangle$) are obtained by averaging over the involved magnetic sublevels. The population of the ground state at thermal equilibrium depends on the number of magnetic sublevels, $P_g = n_g/(n_g+n_n)$.

The laser field of frequency ω and wave number k propagating in the z direction is $\mathbf{E}=2^{-1}\mathbf{u}\mathcal{E}\exp[i(\omega t-kz)]+\text{c.c.}$,

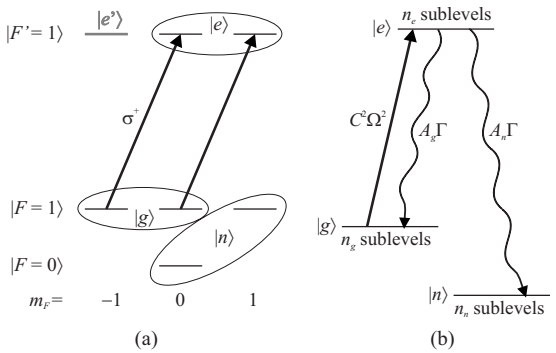

FIG. 1. (a) σ^+ excitation of the $|F=1\rangle \rightarrow |F'=1\rangle$ transition in an atom with nuclear spin $I=1/2$. The magnetic sublevels belonging to each effective energy level are circled. (b) The resulting three-level system.

*thomas.lindvall@tkk.fi

where $\mathbf{u}$ is the polarization vector, $\mathcal{E}$ is the electric-field amplitude, and c.c. stands for complex conjugate. The interaction Hamiltonian in the electric dipole approximation, $V=-\boldsymbol{\mu}\cdot\mathbf{E}$, becomes

$$V=-\hbar\frac{C\Omega}{2}(|e\rangle\langle g|+|g\rangle\langle e|)(e^{i(\omega t-kz)}+e^{-i(\omega t-kz)}). \quad (1)$$

The two-level Rabi frequency is $\Omega=\mu\mathcal{E}/\hbar$, where μ is the dipole moment of a closed transition ($C^2=1$). Instead of taking into account the finite laser beam diameter and collisions with the vapor cell walls in the form of ground-state relaxation, as in [16], we solve the time-dependent evolution equations and average over the distribution of interaction times. As there is no relaxation back from the noncoupled state $|n\rangle$, we can neglect it and treat the system as an open two-level system.

We consider a group of atoms having a longitudinal velocity component v_z described by the density matrix $\rho(v_z,t)$. After a transformation to the rotating frame $\tilde{\rho}_{ge}=\rho_{ge}e^{-i(\omega t-kz)}$ and applying the rotating wave approximation, the evolution equations are, as in [16] but without ground-state relaxation,

$$\frac{d\rho_{ee}}{dt}=-C\Omega\tilde{\rho}_{ge}^{i}-\Gamma\rho_{ee}, \quad (2a)$$

$$\frac{d\rho_{gg}}{dt}=C\Omega\tilde{\rho}_{ge}^{i}+A_g\Gamma\rho_{ee}, \quad (2b)$$

$$\frac{d\tilde{\rho}_{ge}}{dt}=-\left[\frac{\Gamma}{2}+i\delta(v_z)\right]\tilde{\rho}_{ge}+i\frac{C\Omega}{2}(\rho_{ee}-\rho_{gg}). \quad (2c)$$

Here $\tilde{\rho}_{ge}^{i}=\mathrm{Im}(\tilde{\rho}_{ge})$. The laser detuning including the Doppler effect is $\delta(v_z)=\delta_0-kv_z$, where δ_0 is the detuning for an atom at rest. Before the atoms enter the beam at $t=0$ they collide with the cell walls and are in thermal equilibrium [16]. The initial conditions for the density matrix elements are thus $\rho_{gg}=P_g$, $\rho_{ee}=\tilde{\rho}_{ge}=0$. The laser beam is assumed to have a flat-top profile, i.e., its intensity and thus the two-level Rabi frequency Ω are constant within its radius.

Equation (2) can easily be solved by numerically integrating the equation system. Figure 2 shows $-\tilde{\rho}_{ge}^{i}$, upon which the absorption coefficient depends [16], as a function of time for two detunings. We are interested in relatively low intensities, $\Omega\lesssim\Gamma$, at which the time dependence can be divided into three regions: a rapid growth at small t, none or a few heavily damped Rabi oscillations depending on the parameters, and then a slow decay at the optical pumping rate. The slow optical pumping, compared to the atomic lifetime, of several microseconds is in agreement with [14], where saturated absorption spectra were studied.

Since the state of an atom depends on how long it has interacted with the laser field, we must average the density matrix elements over the distribution of interaction times, $p_t(t|v_z)$, that will be derived in Sec. II A,

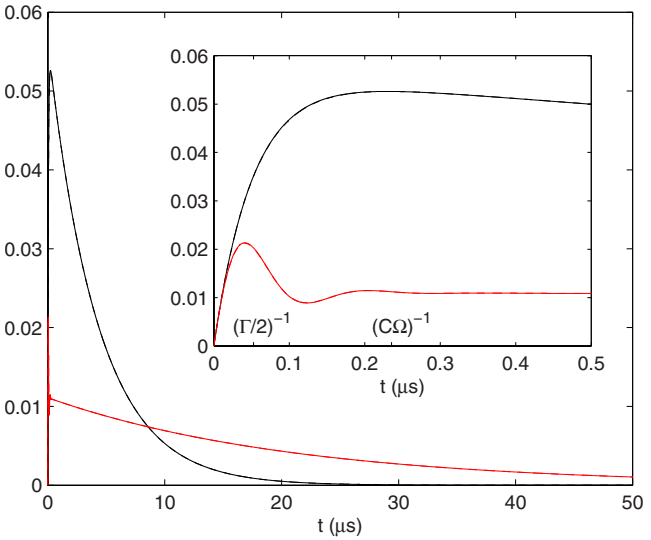

FIG. 2. (Color online) Numerically integrated absorption coefficient (actually $-\tilde{\rho}_{ge}^{i}$) as a function of time for $\delta=0$ (black, upper solid line) and $\delta=\Gamma$ (red, lower solid line). The analytical approximations (black and red dashed lines, respectively) cannot be distinguished from the corresponding numerical curves. The inset shows the initial rise and Rabi oscillations for small t. The time scales $(\Gamma/2)^{-1}$ and $(C\Omega)^{-1}$ are shown. Parameters: $C=P_g=A_g=0.5$, $I/I_s=10^{-1}$, other parameters as for rubidium at $T=300$ K.

$$\langle\rho_{ij}\rangle_t(v_z)=\int_0^\infty\rho_{ij}(v_z,t)p_t(t|v_z)dt. \quad (3)$$

Finally, in order to obtain the Doppler-broadened spectrum of the thermal atomic vapor, we must integrate the result over the longitudinal velocity distribution,

$$\langle\rho_{ij}\rangle_{v_z}=\frac{1}{\sqrt{\pi}v_{\mathrm{mp}}}\int_{-\infty}^{+\infty}\langle\rho_{ij}\rangle_t(v_z)e^{-v_z^2/v_{\mathrm{mp}}^2}dv_z, \quad (4)$$

where $v_{\mathrm{mp}}=\sqrt{2k_BT/m}$ is the most probable velocity of the atoms.

If we obtain the density matrix elements through numerical integration of Eq. (2) and then evaluate integrals (3) and (4) numerically, the calculation of complete absorption spectra will be extremely time consuming and not very convenient for comparison with experimental data. On the other hand, if we can find an approximate solution for Eq. (2), only the two integrals have to be evaluated numerically. Another motivation for finding an approximate analytical solution for ρ is that the numerical solution of Eq. (2) tends to become unstable as the detuning $|\delta|$ increases, unless the integration time step is decreased.

In the following, we will first derive the distribution of interaction times. Then the time-dependent density matrix elements will be solved and averaged over the time and longitudinal velocity distributions.

A. Distribution of interaction times

In our model, the internal state of an atom depends only on how long it has interacted with the laser field. The distri-

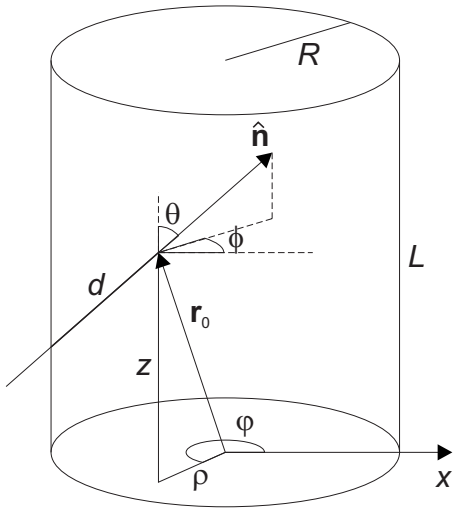

FIG. 3. Geometry of the interaction region. An atom at the position $\mathbf{r}_0$ and traveling in the direction $\hat{\mathbf{n}}$ has traveled the distance d inside the beam.

bution of interaction times can be derived from the beam geometry and the atomic velocity distribution. Harris *et al.* [17] have derived such a distribution from the distribution of path lengths and the velocity distribution of the atoms, but it is not suitable for our purposes because of two reasons. First, it only considers the two transversal dimensions. If a large diameter beam is used, for example, to maximize the signal, a considerable fraction of the atoms will exit the interaction region by colliding with the ends of the glass cell and we need to consider all three dimensions. Second, their distribution is for the total interaction time and corresponds to an experiment where one measures the properties of the atoms as they exit the beam. In a typical absorption or fluorescence measurement, one measures a signal to which all atoms momentarily inside the laser beam contribute. Hence one must integrate also over the spatial distribution of atoms inside the beam. This will be done in the following.

We consider an atom at a position $\mathbf{r}_0=(\rho\cos\varphi,\rho\sin\varphi,z)$ inside the interaction region, defined by the radius R of the laser beam and the length L of the glass cell, see Fig. 3. It is traveling in the direction $\hat{\mathbf{n}}=(\cos\phi\sin\theta,\sin\phi\sin\theta,\cos\theta)$ and has traveled the distance d inside the beam. Depending on $\mathbf{r}_0$ and $\hat{\mathbf{n}}$, it may have entered the beam through the barrel or the end face of the cylinder and the distance d is thus the smaller one of the two distances

$$d_1=\frac{\rho\cos\alpha+\sqrt{R^2-\rho^2\sin^2\alpha}}{\sin\theta}\equiv\frac{\xi}{\sin\theta},\tag{5a}$$

$$d_2=\frac{z}{\cos\theta}.\tag{5b}$$

Because of the circular symmetry of the beam, the uniform distribution of atoms and their isotropic velocity distribution, the distance d_1 depends on the difference $\alpha=\varphi-\phi$ only. We also assume $v_z\geq 0$ as negative velocities would only correspond to flipping the coordinate system. The transversal projection ξ was introduced in Eq. (5a) to keep the expressions more readable.

The uniform spatial distribution of atoms inside the interaction region is

$$p_{(\rho,z)}(\rho,z)=\frac{2\rho}{LR^2}.\tag{6}$$

Since the Doppler shift depends on v_z, we have to use the conditional velocity probability distribution for a fixed v_z,

$$p_{(v_\rho,\alpha)}(v_\rho,\alpha|v_z)=\frac{v_\rho}{\pi v_{\mathrm{mp}}^2}e^{-v_\rho^2/v_{\mathrm{mp}}^2}.\tag{7}$$

This expression is identical to the normal two-dimensional velocity distribution, but for a fixed v_z we have the constraint $v=(v_\rho^2+v_z^2)^{1/2}=d/t$. As $\sin\theta=v_\rho/v$ and $\cos\theta=v_z/v$, we obtain the following two constraints:

$$t_1=\xi/v_\rho,\tag{8a}$$

$$t_2=z/v_z.\tag{8b}$$

The joint spatial and velocity distribution is then

$$p_{(\rho,z,v_\rho,\alpha)}(\rho,z,v_\rho,\alpha|v_z)=p_{\rho,z}(\rho,z)p_{(v_\rho,\alpha)}(v_\rho,\alpha|v_z)$$
$$=\frac{2\rho v_\rho}{\pi LR^2v_{\mathrm{mp}}^2}e^{-v_\rho^2/v_{\mathrm{mp}}^2}.\tag{9}$$

In order to select the correct distance d_j, we introduce a truth function

$$\Theta(T)=\begin{cases}1, & T=\text{true},\\ 0, & T=\text{false}.\end{cases}\tag{10}$$

Using Eq. (5) and the relations $\sin\theta=v_\rho/v$ and $\cos\theta=v_z/v$, the condition $d_1\leq d_2$ corresponds to $z\geq\xi v_z/v_\rho$.

The distribution of interaction times for a fixed v_z is then given by

$$p_t(t|v_z)=\int_0^{2\pi}\int_0^{\infty}\int_0^{L}\int_0^{R}p_{(\rho,z,v_\rho,\alpha)}(\rho,z,v_\rho,\alpha|v_z)$$
$$\times\left[\Theta\left(z<\frac{v_z}{v_\rho}\xi\right)\delta(t-t_2)\right.$$
$$\left.+\Theta\left(z\geq\frac{v_z}{v_\rho}\xi\right)\delta(t-t_1)\right]d\rho dz dv_\rho d\alpha.\tag{11}$$

This expression is evaluated in Appendix A and the result is

$$p_t(t|v_z)=\left[\frac{1}{\tau_{v_z}}\left\{1-e^{-\tau_R^2/t^2}\left[I_0\left(\frac{\tau_R^2}{t^2}\right)+3I_1\left(\frac{\tau_R^2}{t^2}\right)\right]\right\}\right.$$
$$\left.+\frac{2}{t}e^{-\tau_R^2/t^2}I_1\left(\frac{\tau_R^2}{t^2}\right)\right]\Theta(t<\tau_{v_z}),\tag{12}$$

where I_n is the nth order modified Bessel function of the first kind and we have defined the characteristic transversal interaction time $\tau_R=\sqrt{2}R/v_{\mathrm{mp}}$ and the velocity-dependent longitudinal interaction time $\tau_{v_z}=L/|v_z|$. Figure 4 shows this distribution for different velocity groups. Note that if L approaches infinity, only the last term in Eq. (12) remains:

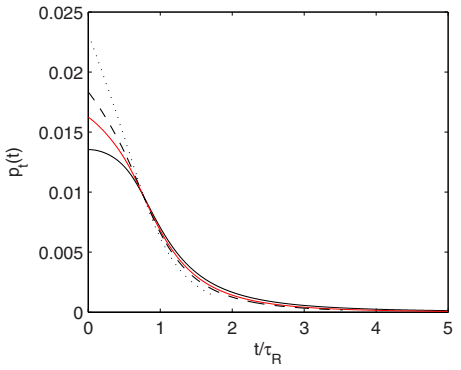

FIG. 4. (Color online) Interaction time distributions $p_t(t|v_z)$ for the velocity groups $v_z=0$ (solid), $v_z=v_{\mathrm{mp}}$ (dashed), and $v_z=2v_{\mathrm{mp}}$ (dotted). The average over v_z, $p_t(t)$, is shown in red (in between the dashed and solid black lines). $R=10$ mm, $L=50$ mm.

the time distribution is independent of longitudinal velocity and identical to the $v_z=0$ distribution in Fig. 4. This is of course exactly the distribution obtained from a two-dimensional treatment. On the other hand, the smaller the ratio L/R, the more the distributions for the different velocity groups will differ.

Even though it is not needed here, it is interesting to calculate the distribution of interaction times averaged over v_z,

$$p_t(t) = \frac{1}{\sqrt{\pi}v_{\mathrm{mp}}}\int_{-\infty}^{+\infty} p_t(t|v_z)e^{-v_z^2/v_{\mathrm{mp}}^2}dv_z$$
$$= \frac{1}{\sqrt{\pi}\tau_L}(1-e^{-\tau_L^2/t^2})\left\{1-e^{-\tau_R^2/t^2}\left[I_0\left(\frac{\tau_R^2}{t^2}\right)+3I_1\left(\frac{\tau_R^2}{t^2}\right)\right]\right\}$$
$$+\frac{2}{t}\mathrm{erf}\left(\frac{\tau_L}{t}\right)e^{-\tau_R^2/t^2}I_1\left(\frac{\tau_R^2}{t^2}\right). \quad (13)$$

Here $\mathrm{erf}(x)$ is the error function and we have defined $\tau_L=L/v_{\mathrm{mp}}$. Also $p_t(t)$ is shown in Fig. 4.

B. Optical pumping rate: first estimate

If we neglect the initial rise and possible Rabi oscillations, we can use an approximation valid for $t \gg \Omega^{-1} \gtrsim \Gamma^{-1}$. We assume that the optical coherence and the excited-state population follow the changes in the ground-state population due to optical pumping so that we can use the steady-state expressions obtained by setting Eqs. (2c) and (2a) equal to zero,

$$\rho_{ee} = \frac{(C\Omega/2)^2}{\delta^2(v_z)+(\Gamma/2)^2+(C\Omega/2)^2}\rho_{gg}, \quad (14a)$$

$$\tilde{\rho}_{ge} = -\frac{[\delta(v_z)+i\Gamma/2]C\Omega/2}{\delta^2(v_z)+(\Gamma/2)^2+(C\Omega/2)^2}\rho_{gg}. \quad (14b)$$

Substituting Eq. (14) into Eq. (2b) yields

$$\frac{d\rho_{gg}}{dt} = -\frac{(C\Omega/2)^2 A_n\Gamma}{\delta^2(v_z)+(\Gamma/2)^2+(C\Omega/2)^2}\rho_{gg}. \quad (15)$$

With the initial condition $\rho_{gg}(t=0)=P_g$, this gives $\rho_{gg}(t)=P_g\exp(-\Gamma_{\mathrm{op,est}}t)$, that is, the ground-state population decays at the optical pumping rate

$$\Gamma_{\mathrm{op,est}} = \frac{(C\Omega/2)^2 A_n\Gamma}{\delta^2(v_z)+(\Gamma/2)^2+(C\Omega/2)^2}. \quad (16)$$

The imaginary part of the optical coherence is then given by

$$\tilde{\rho}_{ge}^i(t) = \tilde{\rho}_{ge,\mathrm{est}}^i e^{-\Gamma_{\mathrm{op,est}}t}, \quad (17)$$

with the initial value

$$\tilde{\rho}_{ge,\mathrm{est}}^i = -\frac{(\Gamma/2)(C\Omega/2)P_g}{\delta^2(v_z)+(\Gamma/2)^2+(C\Omega/2)^2}. \quad (18)$$

We see that expressions (16) and (18) lack the familiar factor of 2 in front of the saturation term in the denominator.

C. Full time dependence

A common way to solve time-dependent density matrix equations is to use the Laplace transform $R(s)=\int_0^\infty \rho(t)e^{-st}dt$. Equation (2) becomes

$$sR_{ee} = -C\Omega R_{ge}^i - \Gamma R_{ee}, \quad (19a)$$

$$sR_{gg} - P_g = C\Omega R_{ge}^i + A_g\Gamma R_{ee}, \quad (19b)$$

$$sR_{ge} = -\left[\frac{\Gamma}{2}+i\delta(v_z)\right]R_{ge} + i\frac{C\Omega}{2}(R_{ee}-R_{gg}), \quad (19c)$$

where the initial conditions $\rho_{gg}(0)=P_g$ and $\rho_{ee}(0)=\tilde{\rho}_{ge}(0)=0$ were used. This algebraic equation system can easily be solved and yields

$$R_{ge}^i(s) = -(s+\Gamma/2)(s+\Gamma)(C\Omega/2)P_g\{s^4+2\Gamma s^3$$
$$+[\delta^2(v_z)+5\Gamma^2/4+(C\Omega)^2]s^2+[\delta^2(v_z)+\Gamma^2/4$$
$$+(1+A_n)(C\Omega)^2/2]\Gamma s+A_n\Gamma^2(C\Omega)^2/4\}^{-1}. \quad (20)$$

If we can solve the roots s_j of the fourth-order polynomial in the denominator, we can write Eq. (20) as a partial fraction $R_{ge}^i(s)=\Sigma_{j=1}^4 B_j/(s-s_j)$, where the coefficients B_j can be solved from $B_j=\lim_{s\to s_j}(s-s_j)R_{ge}^i(s)$. The general time dependence can then be written as

$$\tilde{\rho}_{ge}^i(t) = \sum_{j=1}^4 B_j e^{s_j t}. \quad (21)$$

The exact solution of the fourth-order polynomial in the denominator of Eq. (20) is not very transparent. However, the major contribution to the interaction-time averaged absorption comes from the term in Eq. (21) that describes optical pumping. It is therefore enough to calculate that term as accurately as possibly and include the other ones with a reasonable accuracy to account for the initial rise and Rabi oscillations.

Appendix B describes how to obtain approximative roots and amplitudes and the time dependence can be written as

$$\tilde{\rho}^i_{ge}(t) = \sum_{j=1}^{3} B_j e^{s_j t} = B_1 e^{s_1 t} + 2\,\mathrm{Re}(B_2 e^{s_2 t}), \tag{22}$$

where

$$s_1 = -\frac{A_n \Gamma \left(\frac{C\Omega}{2}\right)^2}{\delta^2(v_z) + \left(\frac{\Gamma}{2}\right)^2 + \left[2 + \frac{\delta^2(v_z) - 3(\Gamma/2)^2}{\delta^2(v_z) + (\Gamma/2)^2} A_n\right]\left(\frac{C\Omega}{2}\right)^2}, \tag{23a}$$

$$s_{2,3} = -\frac{\Gamma}{2} \mp i\delta(v_z) - \frac{A_g \Gamma \pm 2i\delta(v_z)}{\delta^2(v_z) + \left(\frac{\Gamma}{2}\right)^2}\left(\frac{C\Omega}{2}\right)^2, \tag{23b}$$

and

$$B_1 = -\frac{\frac{\Gamma}{2}\frac{C\Omega}{2} P_g}{\delta^2(v_z) + \left(\frac{\Gamma}{2}\right)^2 + \left[2 + \frac{3\delta^2(v_z) - 5(\Gamma/2)^2}{\delta^2(v_z) + (\Gamma/2)^2} A_n\right]\left(\frac{C\Omega}{2}\right)^2}, \tag{24a}$$

$$B_{2,3} = \frac{\frac{1}{2}\left[\frac{\Gamma}{2} \mp i\delta(v_z)\right]\frac{C\Omega}{2} P_g}{\delta^2(v_z) + \left(\frac{\Gamma}{2}\right)^2 + \left[2 + \frac{3\delta^2(v_z) - 5(\Gamma/2)^2}{\delta^2(v_z) + (\Gamma/2)^2} A_n\right]\left(\frac{C\Omega}{2}\right)^2}. \tag{24b}$$

The optical pumping rate is $\Gamma_{\mathrm{op}} = -s_1$. Writing the root s_1 and the amplitudes in this form, we can associate the terms $2(C\Omega/2)^2$ in the denominators with saturation, whereas the terms that are proportional A_n describe the effect of optical pumping. Figure 2 shows that this solution hardly can be distinguished from the numerical solution.

D. Average over interaction-time and velocity distributions

Using Eqs. (22), (23a), (23b), (24a), (24b), and (12) and introducing the dimensionless variables $u = t/\tau_R$, $P_j = -s_j \tau_R$, and $\eta = \tau_{v_z}/\tau_R$, the average over interaction times (3) becomes

$$\langle \tilde{\rho}^i_{ge} \rangle_t(v_z) = \sum_{j=1}^{3} B_j \int_0^{\eta} \left[\frac{1}{\eta}\left\{1 - e^{-1/u^2}\left[I_0\left(\frac{1}{u^2}\right) + 3I_1\left(\frac{1}{u^2}\right)\right]\right\} + \frac{2}{u} e^{-1/u^2} I_1\left(\frac{1}{u^2}\right)\right] e^{-P_j u} du. \tag{25}$$

The integral is a function of the two variables P_j and η only, but can unfortunately not be evaluated in closed form. Hence we have to evaluate this integral as well as the integral over the velocity distribution numerically.

Figure 5 shows homogeneous line shapes for different velocity groups. For a moderate intensity and large beam ($I/I_s = 10^{-1}$ and $R = 10$ mm), the line shape depends strongly on the longitudinal velocity; see Fig. 5(a). The amplitude is much smaller for "slow" atoms that experience more optical pumping, and even when scaled with the velocity distribution, there is a slight dip at zero velocity (right-hand figure). At lower intensity and smaller beam size ($I/I_s = 10^{-3}$ and $R = 1$ mm), the line shape is almost velocity independent and no dip occurs, Fig. 5(b).

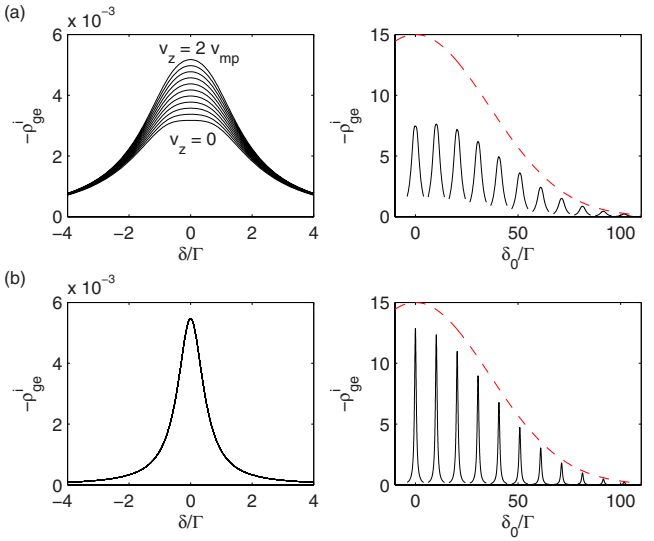

FIG. 5. (Color online) Homogeneous line shapes ($-\tilde{\rho}^i_{ge}$) for the velocity groups $v_z/v_{\mathrm{mp}} = 0, 0.2, \ldots, 2$. The left figures show the line shapes on top of each other, the right figures show the line shapes at their Doppler-shifted positions and scaled by the velocity distribution, which is also shown (red dashed curve, in arbitrary units). (a) $I/I_s = 10^{-1}$, $R = 10$ mm and (b) $I/I_s = 10^{-3}$, $R = 1$ mm. In all figures $C = P_g = A_g = 0.5$, $L = 50$ mm, other parameters as for ^{85}Rb at 300 K.

The absorption coefficient is given by [16]

$$\alpha = -\frac{2kNC\mu}{\varepsilon_0 \mathcal{E}} \langle \tilde{\rho}^i_{ge} \rangle_{v_z}, \tag{26}$$

where N is the number density of the atoms. Figure 6 compares the absorption coefficient obtained by numerically integrating Eq. (22) over t and v_z to the one calculated in [16] for different intensities. The dependence on the beam radius is similar; see Fig. 7.

The behavior of the absorption coefficient can be described using the on-resonance optical pumping rate $\Gamma_{\mathrm{op}}(\delta = 0) \approx A_n (C\Omega)^2/\Gamma$, the inverse of the transversal interaction time $\tau_R^{-1} = v_{\mathrm{mp}}/\sqrt{2}R$, and the ratio of cell length to beam radius L/R. For $L/R \gg 1$ and $\Gamma_{\mathrm{op}}(\delta = 0) \ll \tau_R^{-1}$, the absorption coefficient is practically identical to the result from [16] (see the highest curves in Figs. 6 and 7). When these two rates are of the same order, the difference between the amplitudes is maximum (middle curves in Fig. 6 and second lowest curves in Fig. 7). Keeping the ratio of the two rates constant, the difference increases with intensity. Finally, when $\Gamma_{\mathrm{op}}(\delta = 0) > \tau_R^{-1}$, the amplitudes are again close, but the numerically obtained curve is clearly not a Voigt profile, but has a flatter top or even a dip at the center (lowest curves in Figs. 6 and 7).

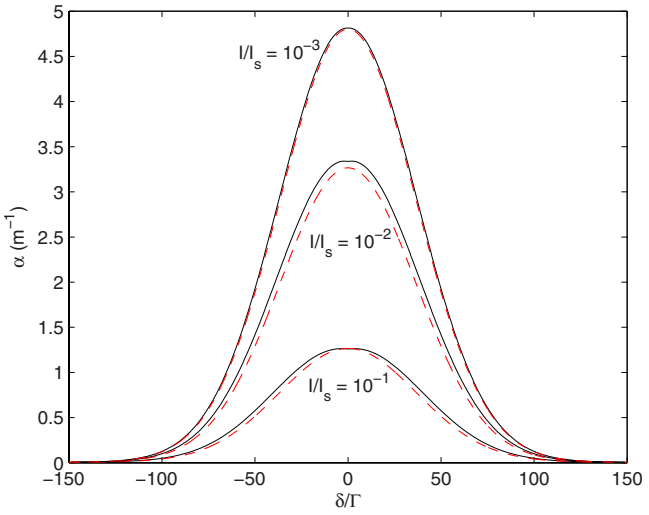

FIG. 6. (Color online) Absorption coefficients obtained from Eq. (22) (black solid curves) and from [16] (red dashed curves) for different intensities. $R=10$ mm, $L=50$ mm, $C=A_g=P_g=0.5$, other parameters as for ^{85}Rb at 300 K.

Figure 8 shows the absorption coefficients for different cell lengths. The result from [16] is always a Voigt profile and the amplitude increases when the length decreases. In the current model, however, atoms with a longitudinal velocity close to zero exit the interaction region mainly in the transversal direction. They are therefore almost unaffected by the cell length, whereas atoms with nonzero longitudinal velocity experience less optical pumping for shorter cell lengths. As the cell length approaches the beam diameter, this causes a dip in the Doppler profile, as anticipated based on Fig. 5(a).

III. RUBIDIUM D_2 SPECTRA

D line spectra for the alkali-metal atoms can be obtained by summing over all transitions between the involved hyperfine levels. As an example, we consider the D_2 spectrum of natural rubidium. The transition frequencies are from [18] and the vapor pressure calculated according to [19]. Other parameters are given in Appendix C.

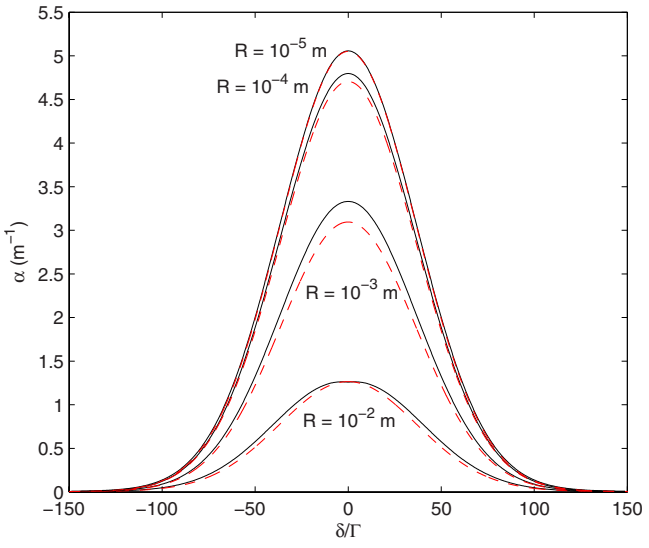

FIG. 7. (Color online) Absorption coefficients obtained from Eq. (22) (black solid curves) and from [16] (red dashed curves) for different beam radii. $I/I_s=0.1$, $L=50$ mm, $C=A_g=P_g=0.5$, other parameters as for ^{85}Rb at 300 K.

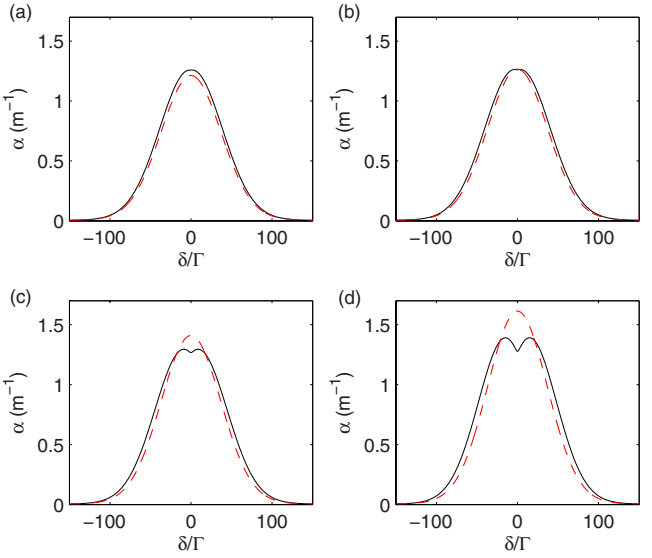

FIG. 8. (Color online) Absorption coefficients obtained from Eq. (22) (black solid curves) and from [16] (red dashed curves) for (a) $L=100$ mm, (b) $L=50$ mm, (c) $L=20$ mm, and (d) $L=10$ mm. $I/I_s=0.1$, $R=10$ mm, $C=A_g=P_g=0.5$, other parameters as for ^{85}Rb at 300 K.

In [16] we took into account that the absorption coefficient depends on the intensity, which decreases along the length of the cell, by formally dividing the cell into many thin slices. However, it was seen that the effect is relatively small and for simplicity it is neglected here.

The dependence of the rubidium spectra on the parameters follows the behavior outlined for a single transition in Sec. II D. Figure 9 shows D_2 spectra for natural rubidium obtained by numerically integrating Eq. (22) compared to the result from [16] and to spectra calculated by neglecting optical pumping but including saturation. In Fig. 9(a) the optical pumping is strong. The differences in line shape seen in Figs. 6 and 7 are not as visible as each Doppler line consists of three overlapping transitions. Figure 9(b) represents the case where $\Gamma_{\mathrm{op}}(\delta=0)\sim\tau_R^{-1}$ and the difference between the two methods of accounting for optical pumping is largest. They are still close compared to the spectrum neglecting optical pumping. Figure 9(c) shows how the two results again approach each other as the optical pumping is reduced when the intensity and beam radius are decreased.

The influence of optical pumping on the absolute absorption on the rubidium D lines has been experimentally studied in a recent paper [15]. The authors measured the spectra using a linearly polarized laser beam without nulling or controlling the laboratory magnetic field. This means that the polarization experienced by the atoms depends on the local field, which consists of the magnetic field of the Earth and the fluctuating fields caused by electronic equipment. Figure 10 shows numerically integrated rubidium D_2 absorption spectra for parameters corresponding to Fig. 6 in [15] and for the following cases: π or σ^+ polarization, σ polarization

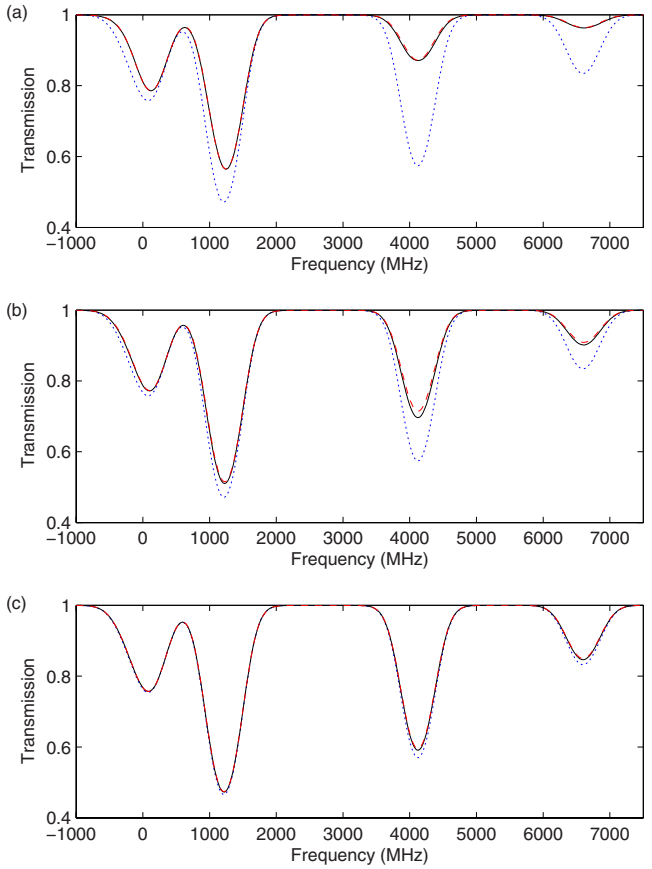

FIG. 9. (Color online) Rubidium D_2 spectra for π or σ^+ polarization obtained from Eq. (22) (black solid curves), from [16] (red dashed curves), and neglecting optical pumping, but including saturation (blue dotted curves). (a) $I/I_s=0.1$, $R=10$ mm, (b) $I/I_s=0.1$, $R=1$ mm, (c) $I/I_s=0.01$, $R=1$ mm. $L=50$ mm, $C=A_g=P_g=0.5$, other parameters as for natural Rb at 300 K.

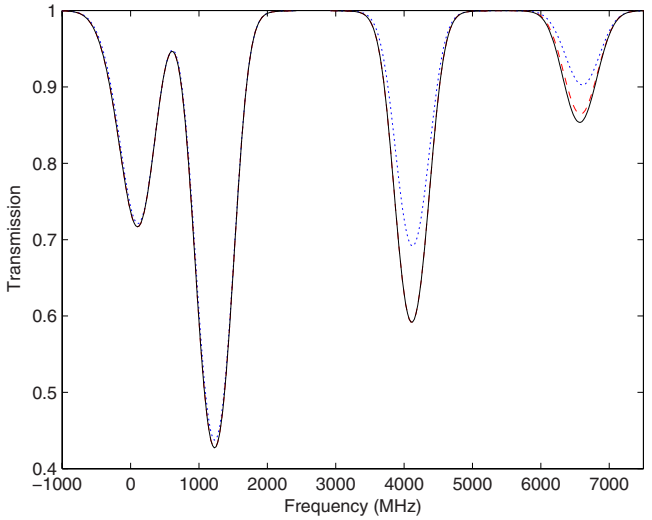

FIG. 10. (Color online) Rubidium D_2 spectra for π or σ^+ polarization (blue dotted curve), σ polarization (red dashed curve), and random quantization axis (black solid curve). $I/I_s=10^{-1}$, $L=75$ mm, $R=2$ mm, and $T=298.55$ K.

(equal amounts of σ^+ and σ^-), and randomly distributed quantization axis (equal amounts of π, σ^+, and σ^-). The more polarization components that are involved, the fewer uncoupled magnetic sublevels there will be in the ground state and the less prominent the optical pumping will be. The only difference between σ and random polarization in this case occurs for the $|F=1\rangle \rightarrow |F'=0\rangle$ transition of the 87A line, where the ground sublevel $m_F=0$ is uncoupled for σ, but coupled for random polarization.

The absolute vapor pressure (number density) must in practice be kept as a free parameter, or be calibrated, because the uncertainty of the empirical formula [19] has been reported to be as high as 1.5 [20]. Taking this into account, the spectrum in Fig. 6 of [15] agrees well with our results for the following parameters: a vapor pressure almost 10% higher than that given by [19] and a polarization which consists of about 80% σ and 20% π.

IV. CONCLUSIONS AND FURTHER RESEARCH

We have shown that the result from [16] is valid over a wide range of parameters and can be used for straightforward comparison with experimental data. The solution obtained by numerically integrating Eq. (22) reveals some additional features and can still be used to plot full spectra, although it is significantly more computer time consuming.

We have also shown how the optical pumping causes atoms with a longitudinal velocity around zero to have clearly non-Lorentzian homogeneous lines. It would thus be interesting to study saturation spectroscopy. It has been studied numerically in [13,14], but analytical (approximative) results may be hard to obtain as the longitudinal intensity dependence of the (partial) standing wave makes it difficult to decouple the transversal and longitudinal motion as was done in this paper.

The effect of the finite laser beam size can be considered as a form of transit-time broadening, which is known to affect the line shape and depend on the intensity distribution of the beam [21]. It would therefore be interesting to study this effect also for other laser beam profiles, in particular a (truncated) Gaussian profile. However, in this case the evolution of an atom does not depend on the interaction time only, but also on the particular path it travels. This would require numerical simulations.

ACKNOWLEDGMENTS

We are thankful to K. Blomstedt for helpful discussions on the mathematical aspects of the paper. This work was supported by the Academy of Finland and the Jenny and Antti Wihuri Foundation.

APPENDIX A: DISTRIBUTION OF INTERACTION TIMES

Substituting Eqs. (8) and (9), Eq. (11) becomes

$$p_t(t|v_z) = \int_0^{2\pi}\int_0^{\infty}\int_0^{L}\int_0^{R} \frac{2\rho v_\rho}{\pi L R^2 v_{\mathrm{mp}}^2} e^{-v_\rho^2/v_{\mathrm{mp}}^2} \left[\Theta\left(z < \frac{v_z}{v_\rho}\xi\right) \times \delta\left(t - \frac{z}{v_z}\right) + \Theta\left(z \geq \frac{v_z}{v_\rho}\xi\right)\delta\left(t - \frac{\xi}{v_\rho}\right)\right] d\rho dz dv_\rho d\alpha. \tag{A1}$$

Using the property $\delta(ax)=\delta(x)/|a|$, one can integrate the first term over z and the second term over v_ρ. One has to pay attention to the relation between the integration limits and the argument of the Θ functions. Further Θ functions can be used to account for the different possible cases. For example, integrating the first term over z gives

$$\begin{aligned}
&\int_0^L \Theta\left(z<\frac{v_z}{v_\rho}\xi\right)v_z\delta(z-v_zt)dz \\
&\quad=v_z\left[\Theta\left(L<\frac{v_z}{v_\rho}\xi\right)\int_0^L\delta(z-v_zt)dz\right. \\
&\qquad\left.+\Theta\left(L\geq\frac{v_z}{v_\rho}\xi\right)\int_0^{v_z/v_\rho\xi}\delta(z-v_zt)dz\right] \\
&\quad=v_z\left[\Theta\left(L<\frac{v_z}{v_\rho}\xi\right)\Theta(v_zt<L)\right. \\
&\qquad\left.+\Theta\left(L\geq\frac{v_z}{v_\rho}\xi\right)\Theta\left(v_zt<\frac{v_z}{v_\rho}\xi\right)\right] \\
&\quad=v_z\Theta\left(v_\rho<\frac{\xi}{t}\right)\Theta(v_zt<L). \qquad \text{(A2)}
\end{aligned}$$

In the last step, we were able to recombine the two terms based on how they limit the possible v_ρ values. We see that the first Θ function gives the upper limit for the integral over v_ρ. The last Θ function will of course be present in the final expression, as the maximum interaction time for the velocity group v_z is equal to $L/|v_z|$.

Integrated over z and v_ρ, Eq. (A1) becomes

$$\begin{aligned}
p_t(t|v_z)=\frac{2\Theta(t<L/v_z)}{\pi LR^2v_{\mathrm{mp}}^2}\int_0^{2\pi}\int_0^R\rho\left\{\frac{v_zv_{\mathrm{mp}}^2}{2}[1-e^{-(\xi/v_{\mathrm{mp}}t)^2}]\right. \\
\left.+\frac{L-v_zt}{t^3}\xi^2e^{-(\xi/v_{\mathrm{mp}}t)^2}\right\}d\rho d\alpha. \qquad \text{(A3)}
\end{aligned}$$

We change integration variables to $y=r\sin\alpha$ and $\xi=\rho\cos\alpha+\sqrt{R^2-\rho^2\sin^2\alpha}$ and can then easily integrate over y,

$$\begin{aligned}
p_t(t|v_z)&=\frac{4\Theta(t<L/v_z)}{\pi LR^2v_{\mathrm{mp}}^2}\int_0^{2R}\int_0^{\sqrt{R^2-\xi^2/4}}\left\{\frac{v_zv_{\mathrm{mp}}^2}{2}[1-e^{-(\xi/v_{\mathrm{mp}}t)^2}]\right. \\
&\quad\left.+\frac{L-v_zt}{t^3}\xi^2e^{-(\xi/v_{\mathrm{mp}}t)^2}\right\}dyd\xi \\
&=\frac{4\Theta(t<L/v_z)}{\pi LR^2v_{\mathrm{mp}}^2}\int_0^{2R}\sqrt{R^2-\frac{\xi^2}{4}}\left\{\frac{v_zv_{\mathrm{mp}}^2}{2}[1-e^{-(\xi/v_{\mathrm{mp}}t)^2}]\right. \\
&\quad\left.+\frac{L-v_zt}{t^3}\xi^2e^{-(\xi/v_{\mathrm{mp}}t)^2}\right\}d\xi. \qquad \text{(A4)}
\end{aligned}$$

One more change in variable, $\cos\beta/2=\xi/2R$, yields the integral

$$\begin{aligned}
p_t(t|v_z)&=\frac{4\Theta(t<L/v_z)}{\pi Lv_{\mathrm{mp}}^2}\int_0^{\pi}\\
&\quad\times\sin^2\frac{\beta}{2}\left\{\frac{v_zv_{\mathrm{mp}}^2}{2}\left[1-\exp\left(-\frac{4R^2\cos^2\frac{\beta}{2}}{v_{\mathrm{mp}}^2t^2}\right)\right]\right. \\
&\quad\left.+\frac{L-v_zt}{t^3}4R^2\cos^2\frac{\beta}{2}\exp\left(-\frac{4R^2\cos^2\frac{\beta}{2}}{v_{\mathrm{mp}}^2t^2}\right)\right\}d\beta. \qquad \text{(A5)}
\end{aligned}$$

Using $\sin^2 x=(1-\cos 2x)/2$ and $\cos^2 x=(1+\cos 2x)/2$, this can be written as

$$\begin{aligned}
p_t(t|v_z)&=\frac{2\Theta(t<L/v_z)}{\pi Lv_{\mathrm{mp}}^2}\int_0^{\pi}\left(\frac{v_zv_{\mathrm{mp}}^2}{2}(1-\cos\beta)\right.\\
&\quad\times\left\{1-\exp\left[-\frac{2R^2}{v_{\mathrm{mp}}^2t^2}(1+\cos\beta)\right]\right\}\\
&\quad+\frac{L-v_zt}{t^3}R^2(1-\cos 2\beta)\\
&\quad\left.\times\exp\left[-\frac{2R^2}{v_{\mathrm{mp}}^2t^2}(1+\cos\beta)\right]\right)d\beta. \qquad \text{(A6)}
\end{aligned}$$

Using the integral representation $I_\nu(z)=\pi^{-1}\int_0^\pi\exp(z\cos\theta)\cos(\nu\theta)d\theta$ [22] for the modified Bessel functions of the first kind and defining the transversal interaction time scale $\tau_R=\sqrt{2}R/v_{\mathrm{mp}}$ and the velocity-dependent longitudinal time scale $\tau_{v_z}=L/|v_z|$, Eq. (A6) becomes

$$\begin{aligned}
p_t(t|v_z)&=\Theta(t<\tau_{v_z})\left(\frac{1}{\tau_{v_z}}\left\{1-e^{-\tau_R^2/t^2}\left[I_0\left(-\frac{\tau_R^2}{t^2}\right)\right.\right.\right.\\
&\quad\left.\left.\left.-I_1\left(-\frac{\tau_R^2}{t^2}\right)\right]\right\}+\frac{\tau_R^2}{t^3}\left(1+\frac{t}{\tau_{v_z}}\right)e^{-\tau_R^2/t^2}\left[I_0\left(-\frac{\tau_R^2}{t^2}\right)\right.\right.\\
&\quad\left.\left.-I_2\left(-\frac{\tau_R^2}{t^2}\right)\right]\right). \qquad \text{(A7)}
\end{aligned}$$

Using the recurrence relation $I_{\nu-1}(z)-I_{\nu+1}(z)=(2\nu/z)I_\nu(z)$ [22], the fact that $I_0(z)$ is even and $I_1(z)$ is odd, and rearranging, Eq. (A7) becomes

$$\begin{aligned}
p_t(t|v_z)&=\left[\frac{1}{\tau_{v_z}}\left\{1-e^{-\tau_R^2/t^2}\left[I_0\left(\frac{\tau_R^2}{t^2}\right)+3I_1\left(\frac{\tau_R^2}{t^2}\right)\right]\right\}\right.\\
&\quad\left.+\frac{2}{t}e^{-\tau_R^2/t^2}I_1\left(\frac{\tau_R^2}{t^2}\right)\right]\Theta(t<\tau_{v_z}). \qquad \text{(A8)}
\end{aligned}$$

This is a convenient form, as $\exp(-|x|)I_1(x)$ is a frequently used function that is available in, for example, MATLAB.

APPENDIX B: FOURTH-ORDER ROOTS

We want to solve the roots of the fourth-order polynomial in the denominator of Eq. (20),

$$s^4 + 2\Gamma s^3 + [\delta^2 + 5\Gamma^2/4 + (C\Omega)^2]s^2 + [\delta^2 + \Gamma^2/4 + (1 + A_n) \times (C\Omega)^2/2]\Gamma s + A_n\Gamma^2(C\Omega)^2/4 = 0. \quad \text{(B1)}$$

The exact solution of Eq. (B1) is not very transparent. An approximate solution valid for $(C\Omega/\Gamma)^2 \ll 1$ can be obtained by substituting a series expansion in $x \equiv (C\Omega/\Gamma)^2$, $s = \Sigma_k s_k x^k$, into Eq. (B1). The first two nonzero terms of the roots are

$$s_1 = -\frac{A_n\Gamma}{\delta^2 + \left(\frac{\Gamma}{2}\right)^2}\left(\frac{C\Omega}{2}\right)^2 + \frac{A_n\Gamma\left[(2 + A_n)\delta^2 + (2 - 3A_n)\left(\frac{\Gamma}{2}\right)^2\right]}{\left[\delta^2 + \left(\frac{\Gamma}{2}\right)^2\right]^3}\left(\frac{C\Omega}{2}\right)^4 + O(x^3), \quad \text{(B2a)}$$

$$s_{2,3} = -\frac{\Gamma}{2} \mp i\delta - \frac{A_g\Gamma \pm 2i\delta}{\delta^2 + \left(\frac{\Gamma}{2}\right)^2}\left(\frac{C\Omega}{2}\right)^2 + O(x^2), \quad \text{(B2b)}$$

$$s_4 = -\Gamma + \frac{(1 + A_g)\Gamma}{\delta^2 + \left(\frac{\Gamma}{2}\right)^2}\left(\frac{C\Omega}{2}\right)^2 + O(x^2). \quad \text{(B2c)}$$

From the original Eq. (2), we see that $s_{2,3}$ are related to the evolution of the optical coherence while s_4 is related to the decay of the excited state. The first root s_1 describes the optical pumping.

If we study the exact roots of Eq. (B1) numerically, we note that for $\delta = 0$ all four roots are real and different. Then, for a certain small value of $|\delta|$, the two roots s_2 and s_3 become degenerate and evolve into a complex conjugate pair. Because the four roots are not distinguishable everywhere, we expect convergence problems for the series solution. Indeed, the x^2 terms of the roots $s_{2,3}$ do diverge for $\delta = 0$.

As mentioned in Sec. II C, we only need s_1 as exactly as possible. The drawback with expression (B2a) is that the $(C\Omega/2)^4$ term does not give much physical insight. We would rather have a $(C\Omega/2)^2$ term in the denominator as in Eq. (16). To achieve this, we use a Padé approximant, which is a rational function whose power series expansion agrees with the series expansion in Eq. (B2a) [23]. Using functions of order x^1 in both the numerator and denominator, we obtain

$$s_{1,\mathrm{P}} = -\frac{A_n\Gamma\left(\frac{C\Omega}{2}\right)^2}{\delta^2 + \left(\frac{\Gamma}{2}\right)^2 + \left[2 + \frac{\delta^2 - 3(\Gamma/2)^2}{\delta^2 + (\Gamma/2)^2}A_n\right]\left(\frac{C\Omega}{2}\right)^2}. \quad \text{(B3)}$$

Using the formula

$$B_j = \lim_{s \to s_j}(s - s_j)R^i_{ge}(s), \quad \text{(B4)}$$

we can obtain the amplitudes for the exponential functions. Using terms up to x^2 for the roots s_j, we obtain

$$B_1 = -\frac{\frac{\Gamma}{2}\frac{C\Omega}{2}P_g}{\delta^2 + \left(\frac{\Gamma}{2}\right)^2 + \left[2 + \frac{3\delta^2 - 5(\Gamma/2)^2}{\delta^2 + (\Gamma/2)^2}A_n\right]\left(\frac{C\Omega}{2}\right)^2}, \quad \text{(B5)}$$

where we have discarded higher-order terms from the denominator. It turns out that Eqs. (B3) and (B5) describe the slow decay due to optical pumping very well.

The amplitudes $B_{2,3}$ are approximately

$$B_{2,3} \approx \frac{\frac{1}{2}\left(\frac{\Gamma}{2} \mp i\delta\right)\frac{C\Omega}{2}P_g}{\delta^2 + \left(\frac{\Gamma}{2}\right)^2}, \quad \text{(B6)}$$

but again the higher-order terms lead to divergence at $\delta = 0$. However, the amplitude B_4 is of the order $(C\Omega/\Gamma)^3$, so it can be neglected compared to B_1 and $B_{2,3}$. Then, since we require $\tilde{\rho}^i_{ge}(0) = B_1 + B_2 + B_3 = B_1 + 2\,\mathrm{Re}(B_2) = 0$, we have to set

$$B_{2,3} = \frac{\frac{1}{2}\left(\frac{\Gamma}{2} \mp i\delta\right)\frac{C\Omega}{2}P_g}{\delta^2 + \left(\frac{\Gamma}{2}\right)^2 + \left[2 + \frac{3\delta^2 - 5(\Gamma/2)^2}{\delta^2 + (\Gamma/2)^2}A_n\right]\left(\frac{C\Omega}{2}\right)^2}. \quad \text{(B7)}$$

We will see that Eq. (B7) together with $s_{2,3}$ as given in Eq. (B2b) describes the initial rise and Rabi oscillations well enough for our purpose.

TABLE I. Numerical parameters for the rubidium D_2 transitions: ground-state populations P_g, branching ratios A_g, and transition strengths C^2 for π or σ^+ and σ polarization.

		π/σ^+			σ		
	Transition	P_g	A_g	C^2	P_g	A_g	C^2
^{87}Rb	$\|1\rangle \to \|0\rangle$	$\frac{1}{8}$	$\frac{40}{120}$	$\frac{120}{360}$	$\frac{2}{8}$	$\frac{80}{120}$	$\frac{60}{360}$
	$\|1\rangle \to \|1\rangle$	$\frac{2}{8}$	$\frac{50}{120}$	$\frac{150}{360}$	$\frac{3}{8}$	$\frac{100}{120}$	$\frac{100}{360}$
	$\|1\rangle \to \|2\rangle$	$\frac{3}{8}$	$\frac{60}{120}$	$\frac{100}{360}$	$\frac{3}{8}$	$\frac{60}{120}$	$\frac{100}{360}$
	$\|2\rangle \to \|1\rangle$	$\frac{3}{8}$	$\frac{12}{120}$	$\frac{20}{360}$	$\frac{5}{8}$	$\frac{20}{120}$	$\frac{12}{360}$
	$\|2\rangle \to \|2\rangle$	$\frac{4}{8}$	$\frac{45}{120}$	$\frac{75}{360}$	$\frac{5}{8}$	$\frac{60}{120}$	$\frac{60}{360}$
	$\|2\rangle \to \|3\rangle$	$\frac{5}{8}$	$\frac{120}{120}$	$\frac{168}{360}$	$\frac{5}{8}$	$\frac{120}{120}$	$\frac{168}{360}$
^{85}Rb	$\|2\rangle \to \|1\rangle$	$\frac{3}{12}$	$\frac{2268}{3780}$	$\frac{3780}{11340}$	$\frac{5}{12}$	$\frac{9}{9}$	$\frac{2268}{11340}$
	$\|2\rangle \to \|2\rangle$	$\frac{4}{12}$	$\frac{2205}{3780}$	$\frac{3675}{11340}$	$\frac{5}{12}$	$\frac{7}{9}$	$\frac{2940}{11340}$
	$\|2\rangle \to \|3\rangle$	$\frac{5}{12}$	$\frac{1680}{3780}$	$\frac{2352}{11340}$	$\frac{5}{12}$	$\frac{4}{9}$	$\frac{2352}{11340}$
	$\|3\rangle \to \|2\rangle$	$\frac{5}{12}$	$\frac{600}{3780}$	$\frac{840}{11340}$	$\frac{7}{12}$	$\frac{2}{9}$	$\frac{600}{11340}$
	$\|3\rangle \to \|3\rangle$	$\frac{6}{12}$	$\frac{1750}{3780}$	$\frac{2450}{11340}$	$\frac{7}{12}$	$\frac{5}{9}$	$\frac{2100}{11340}$
	$\|3\rangle \to \|4\rangle$	$\frac{7}{12}$	$\frac{3780}{3780}$	$\frac{4860}{11340}$	$\frac{7}{12}$	$\frac{9}{9}$	$\frac{4860}{11340}$

APPENDIX C: PARAMETERS FOR RUBIDIUM D_2 LINE

Natural rubidium consists of the isotopes ^{85}Rb (72.17%) with an atomic mass of 84.911 789 74 u and ^{87}Rb (27.83%) with an atomic mass of 86.909 180 53 u [24]. Table I contains the ground-state populations P_g, branching ratios A_g, and transition strengths C^2 for π or σ^+ polarization and σ polarization for all the hyperfine transitions of the D_2 lines of both isotopes. The parameters for randomly distributed quantization axis (equal amounts of π, σ^+, and σ^-) are identical to those for σ polarization, except for the ^{87}Rb $|1\rangle \rightarrow |0\rangle$ transition, for which they are $P_g=3/8$, $A_g=1$, and $C^2=1/9$. The values are obtained by averaging over all involved magnetic sublevels as described in [16]. The strengths of the transitions between the magnetic sublevels are from [25]. For simplicity, we have used the wavelength $\lambda=780$ nm and the natural linewidth $\Gamma=38$ s^{-1} for all transitions in both isotopes corresponding to the dipole moment $\mu=(3\hbar\Gamma\epsilon_0\lambda^3/8\pi^2)^{1/2}\approx 2.5\times 10^{-29}$ Cm.

[1] T. Ikegami, S. Sudo, and Y. Sakai, *Frequency Stabilization of Semiconductor Laser Diodes* (Artech House, Boston, 1995).

[2] J. Vanier, in Recent Advances in Metrology and Fundamental Constants: Proceedings of the International School of Physics "Enrico Fermi," Course CXLVI, edited by T. J. Quinn, S. Leschiutta, and P. Tavella (IOS Press, Amsterdam, 2001), p. 397.

[3] V. Shah, S. Knappe, P. D. D. Schwindt, and J. Kitching, Nat. Photonics **1**, 649 (2007).

[4] S. Chu, Rev. Mod. Phys. **70**, 685 (1998).

[5] C. Cohen-Tannoudji, Rev. Mod. Phys. **70**, 707 (1998).

[6] W. D. Phillips, Rev. Mod. Phys. **70**, 721 (1998).

[7] E. A. Cornell and C. E. Wieman, Rev. Mod. Phys. **74**, 875 (2002).

[8] W. Ketterle, Rev. Mod. Phys. **74**, 1131 (2002).

[9] E. Arimondo, Prog. Opt. **35**, 257 (1996).

[10] R. W. Boyd and D. J. Gauthier, Prog. Opt. **43**, 497 (2002).

[11] W. Happer, Rev. Mod. Phys. **44**, 169 (1972).

[12] J. Vanier, Appl. Phys. B: Lasers Opt. **81**, 421 (2005).

[13] D. A. Smith and I. G. Hughes, Am. J. Phys. **72**, 631 (2004).

[14] L. P. Maguire, R. M. W. van Bijnen, E. Mese, and R. E. Scholten, J. Phys. B **39**, 2709 (2006).

[15] P. Siddons, C. S. Adams, C. Ge, and I. G. Hughes, J. Phys. B **41**, 155004 (2008).

[16] T. Lindvall and I. Tittonen, J. Mod. Opt. **54**, 2779 (2007); J. Mod. Opt. **55**, 2497 (2008).

[17] M. L. Harris, C. S. Adams, S. L. Cornish, I. C. McLeod, E. Tarleton, and I. G. Hughes, Phys. Rev. A **73**, 062509 (2006).

[18] G. P. Barwood, P. Gill, and W. C. R. Rowley, Appl. Phys. B: Lasers Opt. **53**, 142 (1991).

[19] N. A. Nesmeyanov, *Vapor Pressure of the Chemical Elements* (Elsevier, New York, 1963).

[20] A. V. Nowak and B. J. Krohn, IEEE J. Quantum Electron. **21**, 1607 (1985).

[21] W. Demtröder, *Laser Spectroscopy*, 2nd ed. (Springer, Berlin, 1996).

[22] *Handbook of Mathematical Functions with Formulas, Graphs, and Mathematical Tables*, edited by M. Abramowitz and I. A. Stegun (U.S. Government Printing Office, Washington, D.C., 1972).

[23] W. H. Press, S. A. Teukolsky, W. T. Vetterling, and B. P. Flannery, *Numerical Recipes in C*, 2nd ed. (Cambridge University Press, Cambridge, 1992).

[24] *CRC Handbook of Chemistry and Physics*, 89th ed., edited by D. R. Lide (CRC, Boca Raton, 2008).

[25] H. J. Metcalf and P. van der Straten, *Laser Cooling and Trapping* (Springer, New York, 1999).